Journal of Magnetic Resonance 292 (2018) 1–7

Contents lists available at ScienceDirect

Journal of Magnetic Resonance

journal homepage: www.elsevier.com/locate/jmr

Communication

Exploring methods to expedite the recording of CEST datasets using selective pulse excitation

Tairan Yuwen [a,*], Guillaume Bouvignies [b,*], Lewis E. Kay [a,c,*]

[a] Departments of Molecular Genetics, Biochemistry and Chemistry, University of Toronto, Toronto, Ontario M5S 1A8, Canada
[b] Laboratoire des biomolécules, LBM, Département de chimie, École normale supérieure, PSL University, Sorbonne Université, CNRS, 75005 Paris, France
[c] Hospital for Sick Children, Program in Molecular Medicine, 555 University Avenue, Toronto, Ontario M5G 1X8, Canada

ARTICLE INFO

Article history:
Received 4 April 2018
Revised 23 April 2018
Accepted 24 April 2018
Available online 26 April 2018

Keywords:
CEST
cos-modulated waveform
DANTE
Selective excitation
Chemical exchange

ABSTRACT

Chemical Exchange Saturation Transfer (CEST) has emerged as a powerful tool for studies of biomolecular conformational exchange involving the interconversion between a major, visible conformer and one or more minor, invisible states. Applications typically entail recording a large number of 2D datasets, each of which differs in the position of a weak radio frequency field, so as to generate a CEST profile for each nucleus from which the chemical shifts of spins in the invisible state(s) are obtained. Here we compare a number of band-selective CEST schemes for speeding up the process using either DANTE or cosine-modulated excitation approaches. We show that while both are essentially identical for applications such as ^{15}N CEST, in cases where the probed spins are dipolar or scalar coupled to other like spins there can be advantages for the cosine-excitation scheme.

1. Introduction

The development of pulsed Fourier transform (FT) NMR spectroscopy by Ernst and Anderson over 50 years ago [1] has had a profound effect on the types of problems that can be investigated by the NMR technique. The improvements stem directly from the large increase in spectral sensitivity/decreased measurement times associated with pulsed FT NMR relative to the slow-passage frequency sweep approach that predated it. The importance of the pulsed-FT method is underscored by the fact that essentially every modern NMR experiment takes advantage of it [2], yet in at least one class of spin-relaxation experiment, based on Chemical Exchange Saturation Transfer (CEST) [3] and focusing on exchanging systems involving at least one state that is not directly observable, the frequency sweep approach is still commonplace. In this experiment the resonance positions of spins of the often invisible ('excited') state are probed using a weak radio frequency (*rf*) field that is swept through a wide range of frequencies, one at a time, and the effects on the visible ('ground') state monitored by recording a series of spectra, each of which corresponds to a single weak *rf* field position [4,5]. For applications to biomolecular systems, that are of general interest to our laboratory, each spectrum is typically recorded in 2D-mode with as many as 50–100 spectra required, leading to potentially long net acquisition times. Thus, pseudo-3D datasets are obtained where the intensity of each cross-peak, as a function of position of the weak *rf* field, establishes the 3rd (CEST) dimension. In the case of two-site chemical exchange involving the interconversion between conformers corresponding to a highly populated, ground state and a sparsely populated, invisible state a pair of dips is obtained for each spin at the corresponding resonance frequencies of the ground and excited state correlations. Fits of CEST profiles to models of chemical exchange using the Bloch–McConnell equations [6] give estimates of exchange rates, populations and, importantly, chemical shifts of spins in the invisible state [5]. Applications of the methodology to biomolecules such as proteins [7] and nucleic acids [8], exploiting ^{15}N [5], ^{13}C [9–15] or ^{1}H [16–21] reporter spins, are becoming increasingly common.

In an effort to expedite recording of CEST datasets, we have recently described the use of a DANTE-element [22,23] that simultaneously excites multiple regions of the frequency domain, leading to a significant decrease in the frequency range over which the weak *rf* field must be applied in these experiments [24]. In the analogy between pulsed FT and the slow-passage sweep approaches for recording NMR spectra mentioned above the present method corresponds to something in between, whereby a large spectrum is divided into often much smaller subsets, with each subset interrogated simultaneously using a separate sideband

* Corresponding authors.
E-mail addresses: tyuwen@pound.med.utoronto.ca (T. Yuwen), guillaume.bouvignies@ens.fr (G. Bouvignies), kay@pound.med.utoronto.ca (L.E. Kay).

https://doi.org/10.1016/j.jmr.2018.04.013
1090-7807/

of the frequency response of the DANTE element. In the present communication we describe an alternative and related method for decreasing CEST measurement times based on the use of a cosine-modulated CEST waveform (cos-CEST) that in some cases offers distinct advantages over the DANTE-CEST (D-CEST) experiment. The utility of the approach is illustrated with a pair of applications involving ^{1}H- and ^{13}CO-based CEST.

2. Materials and methods

2.1. Sample preparation

A [U-^{15}N] NMR sample of C6A/C57A/C111S/C146S superoxide dismutase (SOD1) that is metal free and reduced (apoSOD1^{2SH}) was prepared as described previously [25], with 1.4 mM protein dissolved in 20 mM HEPES, 1 mM NaN_3, pH 7.4, 90% H_2O/10% D_2O. An NMR sample of [U-^{15}N,^{13}C]-labeled B1 domain of peptostreptococcal protein L (referred to as protein L in what follows) was prepared as described in the literature [10,26], containing 1.5 mM protein dissolved in 50 mM sodium phosphate, 0.05% NaN_3, 90% H_2O/10% D_2O, pH 6.0 buffer.

2.2. NMR spectroscopy

Amide proton cos-CEST and D-CEST experiments were recorded on apoSOD1^{2SH} using an 18.7 T Bruker spectrometer equipped with a z-axis gradient cryogenically cooled probe, 25 °C. An effective weak *rf* field of 30.0 Hz was used during the CEST element (T_{Ex} = 500 ms), corresponding to $\omega_{max}/(2\pi)$ of Eq. (1) for cos-CEST or $B_1^{D\text{-}CEST}\frac{\tau_p}{\tau'}$ for D-CEST, where τ_p is the DANTE pulse width applied at a strength, $B_1^{D\text{-}CEST}$ = 15 kHz, and τ' = $1/sw_{CEST}$ is the duration between DANTE pulses (see below and reference [24]). A range of ^{1}H offsets spanning sw_{CEST} = 1200 Hz (±600 Hz from the center of the amide region, ~8.5 ppm) was chosen, along with N = 3 for the cos-CEST experiment; the position of the weak *rf* carrier was shifted by 30 Hz in each 2D dataset. A second cos-CEST experiment was recorded with all parameters kept the same but with sw_{CEST} = 1260 Hz (±630 Hz from the center of the amide region) to unambiguously determine the amide ^{1}H chemical shifts of the excited state. Each 2D dataset was recorded with 2 transients/FID, a relaxation delay of 0 s and (768, 64) complex points in (t_2, t_1) to give a net acquisition time of ~3 min/spectrum. The total measurement time for each experiment was ~4 h. In principle, it is possible to record each dataset in half the time by sweeping the carrier position between frequencies of $600-k\times60$, $0\le k\le20$, and $630-p\times60$, $0\le p\le21$, about the center of the amide proton region, for the two data sets. Since both datasets are subsequently fit simultaneously (see below), taken together all data points correspond to a frequency spacing of 30 Hz. However, this was not done here. Finally, it is important to emphasize that it is difficult to extract exchange parameters from ^{1}H-CEST experiments because of ^{1}H–^{1}H cross-relaxation effects that distort the sizes of the dips [16]. In the general case, such as for applications involving ^{15}N-CEST, where accurate exchange parameters can be obtained [5], we recommend recording a pair of datasets with different weak *rf* field strengths [7].

^{13}CO cos- and D-CEST experiments were recorded on a protein L sample, 25 °C and 18.7 T. The pulse scheme was identical to a previously published ^{13}CO CEST experiment [9] except that the normal CEST element was replaced with cos- or DANTE-schemes. An effective weak *rf* field of 40.0 Hz was used, T_{Ex} = 400 ms, DANTE pulses were applied using a 10 kHz field (D-CEST) or N = 11 (cos-CEST, Eq. (1)). An 800 Hz range of ^{13}CO offsets centered about 176 ppm was spanned in step sizes of 10 Hz. Each 2D dataset was recorded with 2 transients/FID, a relaxation delay of 2 s and (768, 40) complex points in (t_2, t_1) to give a net acquisition time of ~7 min/spectrum. The total measurement time for each experiment was ~9 h.

2.3. Data analysis

NMR spectra were processed and analyzed using the *NMRPipe* suite of programs [27], with peak intensities extracted with the *autofit* subroutine. CEST profiles were analyzed using the software package *ChemEx* (https://github.com/gbouvignies/chemex), with separate modules for fitting the ^{1}H and ^{13}CO D-CEST and cos-CEST data. These are available from the authors upon request. Only $\Delta\varpi_{GE}$ values were extracted from the analysis of the apoSOD1^{2SH} data, without estimation of the population of the excited state or the rate of exchange between interconverting states, due to ^{1}H–^{1}H cross-relaxation effects that introduce errors in the extracted values, as discussed previously [16]. In the ^{13}CO CEST application to protein L only ground state peaks were observed, as expected from previous studies of this system [28].

3. Results and discussion

Fig. 1, top row, illustrates a number of different CEST schemes in 1D mode, along with the corresponding *rf* amplitude *vs* time domain profiles (center) and the resulting frequency domain excitation profiles (bottom). In Fig. 1A the basic experiment that uses a continuous-wave (CW) excitation element (A, top) is shown, with excitation proceeding one point at a time in the frequency domain (A, bottom). Ultimately a set of spectra is recorded, covering a spectral width, *sw*, which includes all possible resonance positions for the spins of interest. Fig. 1A (bottom) shows the position of the *rf* for the first of the k points that will be recorded in the CEST dimension (blue vertical), along with a horizontal arrow (green) that points along the direction that the *rf* field takes in recording subsequent points. The center of the spectral region probed is indicated with a red dot. Typically, points are recorded that are separated by ~ν_1, where ν_1 is the strength of the weak *rf* field in Hz (referred to in what follows as B_1^{CEST}) [7]. Fig. 1B illustrates the D-CEST method that exploits a DANTE-element to excite magnetization at regularly spaced intervals in frequency space (bottom) [24]. In this implementation a series of (relatively) high power *rf* pulses of duration τ_p are spaced evenly at intervals of τ'. As discussed in detail previously, the DANTE element generates an excitation profile with narrow maxima at frequencies of $\pm p/\tau'$ from the carrier, where p is a whole number [22,23]. Thus, the complete spectrum of interest, that includes all possible chemical shifts for the nucleus in question, *sw*, can be covered by scanning over a range of $1/\tau'$= sw_{CEST} (dark orange-colored region and dark green arrow) where sw_{CEST} < *sw*, leading to measurement times that are reduced by a factor of sw/sw_{CEST}. As with other DANTE applications $\tau_p \ll \tau'$ [22,23], and the strength of the *rf* field is adjusted such that $B_1^{D\text{-}CEST}\frac{\tau_p}{\tau'} = B_1^{CEST}$ so that the net rotation of magnetization in CEST and D-CEST experiments is the same [24]. Notably, the excitation profile can extend far beyond the region of interest, *sw*, (Fig. 1B, bottom) although in many applications, such as for ^{15}N-CEST, this is a non-issue. In contrast, in applications such as amide ^{1}H-CEST [19,20] or ^{13}CO-CEST [9] using samples that are fully protonated (amide ^{1}H-CEST) or [U-^{13}C]-labeled (^{13}CO-CEST) the broad-banded nature of the excitation profile can be problematic, as described below.

Here we introduce an approach related to D-CEST that achieves the desired reduction in CEST measurement times with increased selectivity of the region excited, illustrated in Fig. 1C. Rather than using a DANTE-excitation element a weak continuous *rf* excitation field is exploited that is constructed from a series of cosine functions as

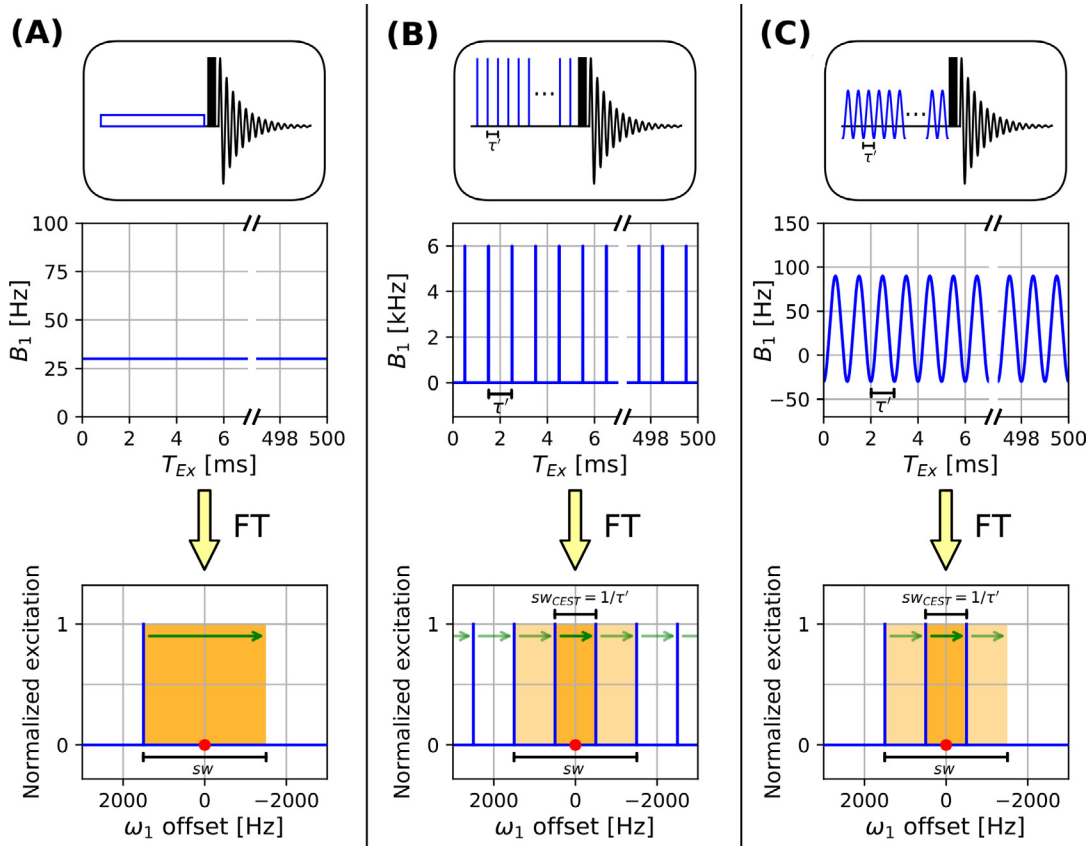

Fig. 1. Comparison of (A) CEST with excitation achieved via a weak CW field (30 Hz), (B) D-CEST where the excitation scheme is a DANTE element [22,23], comprising high power short pulses separated by delay τ' ($B_1^{D\text{-}CEST}\frac{\tau_p}{\tau'} = 30$ Hz) or (C) cos-CEST where the excitation element is an *rf* field given by Eq. (1) with $N = 3$, $\omega_{max}/(2\pi) = 30$ Hz. A value of $sw_{CEST} = 1/\tau' = 1000$ Hz ($\tau' = 1$ ms) was used in (B) and (C). The *rf* carrier is swept *sw* in (A) (dark green arrow), with a spectrum recorded for each frequency, but only sw_{CEST} in (B) and (C), from $+sw_{CEST}/2$ to $-sw_{CEST}/2$, corresponding to a time-savings of sw/sw_{CEST}. Further details are provided in the text. (For interpretation of the references to colour in this figure legend, the reader is referred to the web version of this article.)

$$\boldsymbol{\omega}(t) = \boldsymbol{\omega}_{\max} \sum_{p=-(N-1)/2}^{(N-1)/2} \cos(p2\pi sw_{CEST}t). \tag{1}$$

In Eq. (1) N is the number of excitation frequencies in the waveform, covering only the spectral region of interest (*sw*), Fig. 1C (bottom), ω_{max} is the *rf* amplitude associated with each frequency with $\omega_{max} \ll 2\pi sw_{CEST}$ so that each excitation element is effectively independent of the others. Thus, for $N = 3$, the example considered in Fig. 1C, a series of three selective pulses are applied at frequencies of $\pm sw_{CEST}$ and 0 from the carrier, whose initial position is at $+sw_{CEST}/2$ from the center of the spectrum. In this case the *rf* carrier is 'physically' swept from $+sw_{CEST}/2$ to $-sw_{CEST}/2$ (dark orange-colored region and dark green arrow), about the center of the *sw* range that is to be covered (red dot), one spectrum at a time. However, as 3 frequencies are used in the waveform, a total *sw* of $3sw_{CEST}$ is 'scanned' during this process, corresponding to a savings in measurement time of a factor of 3 over an approach in which the full *sw* is navigated by a single *rf* field. We refer to this experiment as cos-CEST since a series of excitation frequencies is encoded in a cosine-based excitation waveform, although it is clear that a complex waveform comprised of a series of exponentials of the form $\exp(ip2\pi sw_{CEST}t)$ could be used as well.

Fig. 2 shows $\omega(t)$ profiles for $N = 1$, 3, 11 and 1001 generated from Eq. (1), illustrating that as $N \to \infty$ the D-CEST and cos-CEST excitation schemes become equivalent (for $B_1^{D\text{-}CEST} \to \infty$ such that $\tau_p \to 0$). Conversely, in the limit that $N \to 1$ (cos-CEST) or $\tau_p \to \tau'$ (D-CEST) all three approaches converge. A difference between the three experiments, however, relates to the power that is deposited in the probe in each scheme. In what follows we assume that *rf* powers are adjusted so that the net rotation of excited magnetization for the duration of the CEST element is the same in all cases. Thus, it follows that

$$B_1^{D\text{-}CEST}\boldsymbol{\tau}_p = B_1^{CEST}\boldsymbol{\tau}' \tag{2}$$

for D-CEST and CEST, and since the average power in the D-CEST and CEST experiments is given by

$$\begin{aligned} P_{avg}^{D\text{-}CEST} &= \lambda\left(B_1^{D\text{-}CEST}\right)^2\frac{\boldsymbol{\tau}_p}{\boldsymbol{\tau}'} \\ P_{avg}^{CEST} &= \lambda\left(B_1^{CEST}\right)^2 \end{aligned} \tag{3}$$

where λ is a constant, the relative average powers are related according to [24]

$$\frac{P_{avg}^{D\text{-}CEST}}{P_{avg}^{CEST}} = \frac{B_1^{D\text{-}CEST}}{B_1^{CEST}}. \tag{4}$$

In the cos-CEST approach a series of N weak, non-interfering *rf* fields is applied so that

$$\frac{P_{avg}^{\text{cos-}CEST}}{P_{avg}^{CEST}} = N. \tag{5}$$

For ^{15}N studies, for example, and assuming typical B_1 values for ^{15}N CEST (B_1^{CEST}) and ^{15}N D-CEST ($B_1^{D\text{-}CEST}$) of 25 Hz and 6 kHz, respectively, $\frac{P_{avg}^{D\text{-}CEST}}{P_{avg}^{CEST}} \sim 240$. Further, again focusing on ^{15}N applica-

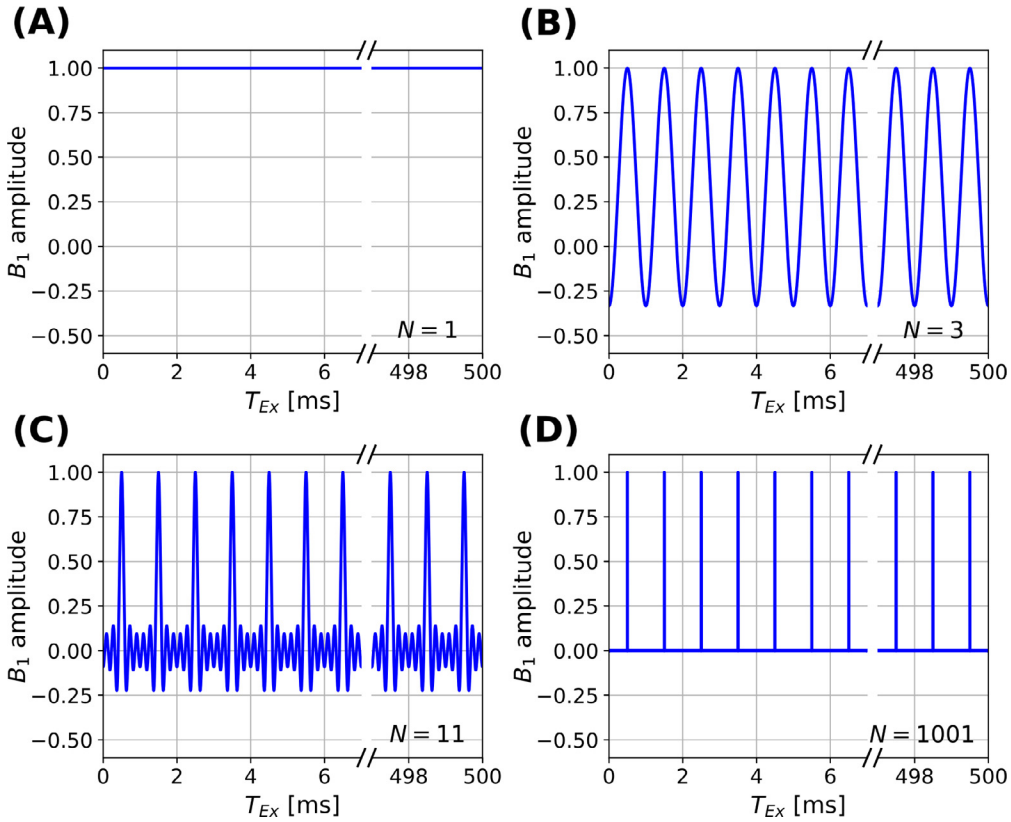

Fig. 2. Examples of cos-excitation elements (Eq. (1)), with $N = 1, 3, 11$ and 1001. Note that as $N \to \infty$ the cos- and D-CEST approaches become identical (for $B_1^{D\text{-}CEST} \to \infty$ such that $\tau_p \to 0$). In all examples the B_1 amplitude is normalized by N. For ease of visualization the excitation functions have been shifted by $\tau'/2 = 0.5$ ms from the time profile given by Eq. (1).

tions where *sw* is on the order of 2400 Hz (18.7 T field) and for $sw_{CEST} = 800$ Hz, $N = 3$ so that $\frac{P_{avg}^{cos\text{-}CEST}}{P_{avg}^{CEST}} = 3$. None of the power requirements for the three classes of CEST experiment is exorbitant as P_{avg}^{CEST} =1.5 mW for a 25 Hz pulse on our cryo-probe. However, it is clear that the power dissipated by the D-CEST scheme is higher than for the cos-CEST sequence, as many more sidebands than necessary are produced via the DANTE approach (Fig. 1). Although we record D-CEST experiments using the highest power settings for the DANTE pulses, this is not a requirement and simulations presented elsewhere show that $B_1^{D\text{-}CEST}$ fields can be reduced by as much as an order of magnitude with no decrease in performance, decreasing the power dissipation by ten-fold as well [24].

For many applications there is essentially no difference in the performance of D-CEST and cos-CEST. In these cases the D-CEST approach may be preferred as it is much faster to fit the resulting data since only a pair of propagators is required, corresponding to evolution with and without the DANTE pulse, while each point of the cos-waveform must be evaluated in the analysis of cos-CEST data. However, in certain cases the fact that the excitation sidebands reside exclusively in the desired *sw* region for cos-CEST is advantageous both in terms of improvements in sensitivity and elimination of artifacts. This is the case for both ^{1}H and ^{13}C applications involving fully protonated (^{1}H-CEST) or fully ^{13}C-labeled (^{13}CO-CEST) samples, where excitation of spins outside the region of interest can be deleterious. By means of example, we consider first the amide proton CEST pulse scheme of Fig. 3 that is optimized for studies of fully protonated exchanging protein systems, using longitudinal relaxation optimized spectroscopy [29], and patterned after the BEST-family of experiments [30]. This sequence follows closely an experiment that we previously published for studies involving highly protonated proteins [19]. However, unlike that

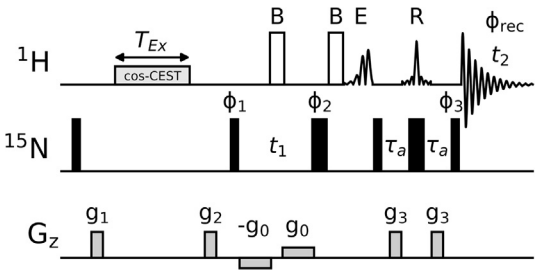

Fig. 3. IPAP-based L-optimized ^{1}H-CEST (BEST-CEST) experiment for the study of slow chemical exchange processes in fully protonated proteins. 90° (180°) rectangular pulses on the ^{15}N channel (119 ppm), denoted by narrow (wide) black rectangles respectively, are applied at maximum power. The pulses on the ^{1}H channel are, in order of execution, BIP [35], EBURP, and REBURP [36], denoted as B, E, R with the actual shapes shown in the pulse diagram. EBURP and REBURP pulses are generated with phase modulation for off-resonance excitation and excite only the amide region of the ^{1}H spectrum (centered at ~8.5 ppm). Typical durations of the shaped pulses (800 MHz) are: BIP: 150 μs; EBURP: 1.44 ms; REBURP: 1.52 ms, that results in ~4 ppm excitation [37]. The ^{1}H carrier is positioned on the water resonance, with the exception of the CEST element. CEST excitation is achieved using a cosine-modulated waveform, given by Eq. (1). The number of frequencies, *N*, in Eq. (1), is chosen such that $N = sw/sw_{CEST}$, where *sw* is the total spectral region that would be swept using CW excitation. The delays used are: $\tau_a \simeq 1/(4^1J_{NH}) = 2.68$ ms. All pulses are applied with phase x unless otherwise indicated. The following phase cycle is used: $\phi_1 = x, -x$; $\phi_2 = 2(x), 2(y), 2(-x), 2(-y)$; $\phi_{rec} = x, -x, -x, x$. Quadrature detection in F_1 is achieved by States-TPPI of ϕ_1 [38]. The IPAP-type acquisition is based on a published SOFAST-HMQC scheme [31] that avoids ^{15}N decoupling during acquisition and achieves the same intrinsic sensitivity as a regular unenhanced HSQC with ^{15}N decoupling during t_2. This is achieved by recording two separate datasets with $\phi_3 = y$ and $\phi_3 = -y$, respectively, that are then processed as described in Supporting Information. The minimum phase cycle is 2. Gradients are applied with the following durations (ms) and strengths (% maximum): g_0: 0.25%, g_1: (0.4, −25%), g_2: (1.0, 15%), g_3: (0.8, 80%). The weak ^{1}H B_1 field was calibrated using the approach of Guenneugues et al. [39]. Note that Asn/Gln sidechain peaks display a 1:2:1 triplet structure in F_2 in the final processed spectrum [31]; an NH_2 purge filter can be included in order to eliminate signals originating from NH_2 groups (see Fig. S3).

sequence where a spin-state selective approach was necessary for the elimination of NOE dips, in the present case NOE dips are removed through the selection of longitudinal two-spin order at the end of a CEST element that starts with longitudinal magnetization [20]. This scheme yields improved sensitivity relative to the spin-state selection method due to its shorter duration. Because the aliphatic reservoir of ^{1}H magnetization is unperturbed during the course of the experiment and can be used to expedite the recovery of the desired amide ^{1}H magnetization, short inter-scan delays can be used. We prefer, therefore, not to employ ^{15}N decoupling and, instead, take advantage of a sensitivity-enhanced approach proposed by Brutscher and coworkers [31] whereby both cosine and sine modulated t_1 components are recorded in each scan, with IPAP virtual decoupling [32,33]. In the absence of relaxation and pulse imperfections the sensitivity of the resultant dataset is equivalent to that recorded using the conventional HSQC approach with decoupling during acquisition.

Fig. 4 compares selected CEST traces obtained from cos-CEST (green) and D-CEST (magenta) experiments recorded on a fully protonated ^{15}N-labeled sample of the antioxidant metalloenzyme superoxide dismutase (SOD1) that lacks stabilizing metal ions and a disulfide bond, apoSOD1^{2SH} [25]. The anti-phase nature of the major and minor dips, corresponding to the negative(positive) intensities of ^{1}H multiplet components for proton magnetization coupled to ^{15}N spin $\alpha(\beta)$, is the result of selecting for longitudinal two-spin order at the end of a CEST element that starts from longitudinal magnetization [20]. Similar shaped profiles are also obtained by taking the difference between separate ^{15}N spin-state selective amide proton CEST traces that also leads to the removal of NOE dips [16]. Notably, significant sensitivity gains are realized for the cos-CEST approach because only amide protons are perturbed by this selective excitation scheme, with aliphatic protons therefore available for use as a magnetization reservoir to increase the recovery rate of the amides. In contrast, the broad-banded nature of the DANTE-excitation results in (partial) saturation of all ^{1}H spins (including water) that therefore decreases the recovery of amide magnetization to its equilibrium value, resulting in a loss of sensitivity. It is worth noting that, in general, it is not possible to achieve a narrower band-width of excitation using D-CEST simply by decreasing $B_1^{D\text{-}CEST}$ to very low values, as

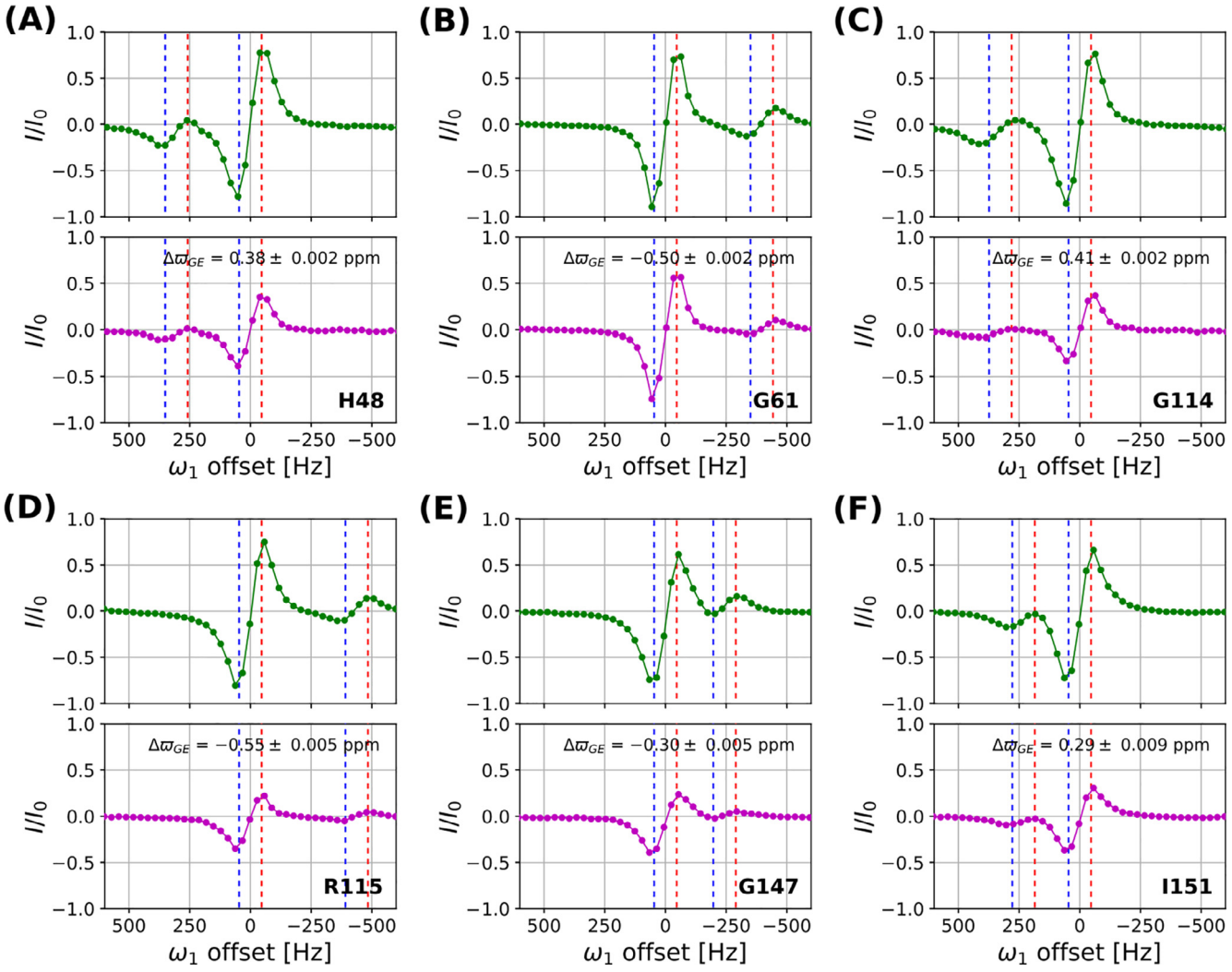

Fig. 4. Representative ^{1}H cos-CEST (green, top; $N = 3$, $\omega_{max}/(2\pi) = 30$ Hz) and D-CEST (magenta, bottom; 15 kHz DANTE pulses) profiles recorded on a sample of fully protonated apoSOD1^{2SH}, 25 °C, 18.7 T, using the pulse sequence of Fig. 3, $sw_{CEST} = 1200$ Hz, $T_{Ex} = 500$ ms. Blue (red) dashed lines denote the positions of multiplet components corresponding to ^{15}N $\alpha(\beta)$ spins. Chemical shift differences between ground (G) and excited (E) states, $\Delta\varpi_{GE}$ are given. Intensities from both cos- and D-CEST profiles are normalized relative to the same reference plane to allow direct comparison. Due to the intrinsic periodic nature of the cos-CEST and D-CEST profiles, a circular shift has been performed such that the ground state position is shifted to ω_1 offset = 0 (the center of each plot). Since there is no aliasing of major and minor dips in these cases, and $|\Delta\nu_{GE}| < |sw_{CEST}/2|$ for all selected residues, the relative position between ground and excited state peaks is properly reflected in each plot. (For interpretation of the references to colour in this figure legend, the reader is referred to the web version of this article.)

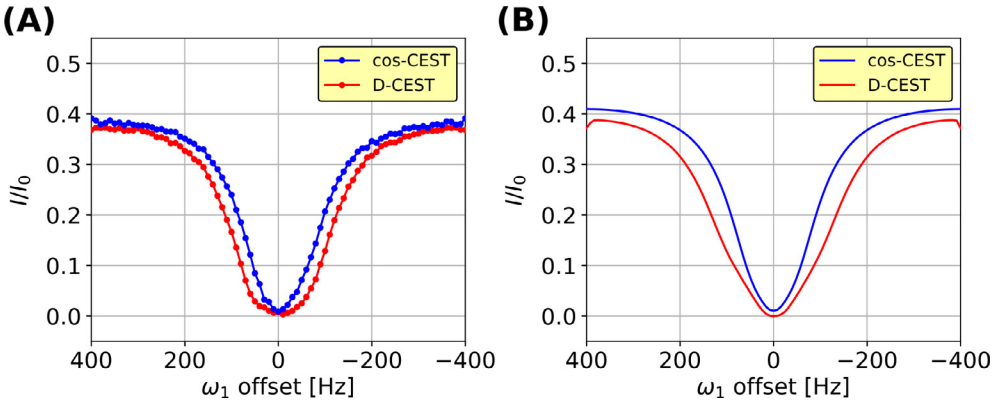

Fig. 5. (A) Experimental CEST profile for Glu 44 of protein L, 25 °C, 18.7 T, recorded using a previously published ^{13}CO-CEST sequence [9], with the CW excitation element replaced by cos- (Eq. (1), $\omega_{max}/(2\pi)$ = 40 Hz, N = 11; blue) or D-CEST (10 kHz DANTE pulses; red) schemes. A value of sw_{CEST} = 800 Hz, corresponding to τ' = 1.25 ms, was used along with T_{Ex} = 400 ms. A circular shift has been performed such that the ground state position is placed at the center of the plot. (B) Simulation of cos-CEST and D-CEST profiles for a ^{13}CO–^{13}C$^{\alpha}$ spin-pair with $^{1}J_{CO\text{-}C\alpha}$ = 55 Hz. All parameters in the simulations are as used experimentally along with R_1 = 2 s^{-1}, R_2 = 10 s^{-1}. The frequency difference Δ between ^{13}CO and ^{13}C$^{\alpha}$ spins was set to 24005 Hz = $k\times sw_{CEST}$ + 5 Hz where k = 30. (For interpretation of the references to colour in this figure legend, the reader is referred to the web version of this article.)

the excitation sidebands still perturb magnetization far from the carrier (Fig. S1). Moreover, simulations show that there can be large distortions to the intensities of the minor state CEST dips in some cases when low $B_1^{D\text{-}CEST}$ fields are used [24].

As discussed in detail in the context of D-CEST, sweeping the carrier over a frequency range $sw_{CEST} < sw$ (here sw_{CEST} =1200 Hz was used) does potentially lead to ambiguities in measured chemical shifts of the excited state, as the shifts may reside outside of the sw_{CEST} window (in regions colored in light orange in Fig. 1). In this case dips are aliased into the sw_{CEST} region [24]. The correct shift can be readily obtained by recording a second dataset with a different sw_{CEST}, in this case sw_{CEST} = 1260 Hz and all other parameters the same. A simultaneous fit of dips in the two profiles measured in this way then provides an accurate chemical shift value, as described previously [24]. Notably, chemical shift differences between ground and excited states for the amide protons of apoSOD1^{2SH} extracted from the cos-CEST and CW-CEST approaches are in excellent agreement, as illustrated in Fig. S2.

We have also recorded ^{13}CO-CEST profiles on a [U-^{15}N,^{13}C]-labeled sample of protein L using a previously published pulse sequence [9] where the CW-CEST element was substituted by either cos-CEST or D-CEST excitation schemes. Fig. 5A compares major dip profiles for Glu 44 (no exchange was observed for this system), with a narrower dip observed for the cos-CEST based method. We have reproduced, through simulation using the Bloch equations, a similar pair of profiles as observed experimentally, Fig. 5B, considering an isolated ^{13}CO–^{13}C$^{\alpha}$ spin-pair. The difference between cos-CEST and D-CEST can be explained by the large one-bond ^{13}CO–^{13}C$^{\alpha}$ scalar coupling that leads to (partial) cross-polarization between ^{13}CO and ^{13}C$^{\alpha}$ spins in the case of D-CEST when the difference between ^{13}CO and ^{13}C$^{\alpha}$ chemical shifts for a given residue, Δ, corresponds very closely to a multiple of sw_{CEST}. In this case the coupled ^{13}CO and ^{13}C$^{\alpha}$ spins are perturbed at the same time by separate DANTE sidebands, giving rise to ^{13}CO magnetization losses and hence less intensity. The effect is very sensitive to Δ so that for a sideband on-resonance with the ^{13}CO spin and a second sideband 10–15 Hz off-resonance for the ^{13}C$^{\alpha}$ spin the effect is small, explaining why we have only observed differences in CEST profiles like the one in Fig. 5A for a small number of residues in protein L.

Finally, we have considered whether a band-selective approach might be useful in studies of chemical exchange via DEST [34]. In applications that exploit CEST, where linewidths of resonances associated with the sparse state tend to be relatively small, the use of multiple excitation side-bands 'speeds-up' the search for the invisible resonances by significantly limiting the region of frequency space that must be examined (small sw_{CEST}). In contrast, studies involving DEST focus on exchange with rare states where linewidths can be many thousands of Hz, necessitating large values for sw_{CEST}, and where the position of the excited state resonance is not in question. It is not clear, therefore, that there would be any advantage in using a D-DEST or cos-DEST approach, especially if parts of a broad line were to be aliased. Further, simulations show that the effect of multiple side-bands simultaneously 'hitting' a broad line of the excited state results in DEST profiles of low sensitivity (intensities not far from zero across the complete DEST profile).

In summary, this work and that described in a companion paper [24] shows that significant time-savings can be achieved using selective-excitation CEST schemes. Here we have focused on the use of cos-modulated excitation fields. These offer some advantages over the DANTE sequence presented elsewhere in systems where the probe spins in question are dipolar or scalar coupled to like spins that can therefore be simultaneously perturbed by the broad-banded nature of the DANTE element. It is expected that the considerable time-savings of D- and cos-CEST will stimulate the development of new CEST experiments with very weak B_1 fields (< 10 Hz) to probe exchanging systems with chemical shift differences that are below the present limits of detection, allowing more subtle conformational changes to be examined than is feasible using the traditional CW experiment.

Acknowledgments

This work was supported by a grant from the Canadian Institutes of Health Research (CIHR; L.E.K.) and with financial support from the French National Center for Scientific Research (CNRS; G.B.). T.Y. acknowledges post-doctoral support from the CIHR. L.E.K. holds a Canada Research Chair in Biochemistry.

Appendix A. Supplementary material

Supplementary data associated with this article can be found, in the online version, at https://doi.org/10.1016/j.jmr.2018.04.013.

References

[1] R.R. Ernst, W.A. Anderson, Application of Fourier transform spectroscopy to magnetic resonance, Rev. Sci. Instrum. 37 (1966) 93–102.
[2] R.R. Ernst, G. Bodenhausen, A. Wokaun, Principles of Nuclear Magnetic Resonance in One and Two Dimensions, Clarendon Press, Oxford, 1987.
[3] S. Forsen, R.A. Hoffman, Study of moderately rapid chemical exchange reactions by means of nuclear magnetic double resonance, J. Chem. Phys. 39 (1963) 2892–2901.
[4] N.J. Anthis, G.M. Clore, Visualizing transient dark states by NMR spectroscopy, Q. Rev. Biophys. 48 (2015) 35–116.
[5] P. Vallurupalli, G. Bouvignies, L.E. Kay, Studying "invisible" excited protein states in slow exchange with a major state conformation, J. Am. Chem. Soc. 134 (2012) 8148–8161.
[6] H.M. McConnell, Reaction rates by nuclear magnetic resonance, J. Chem. Phys. 28 (1958) 430–431.
[7] P. Vallurupalli, A. Sekhar, T. Yuwen, L.E. Kay, Probing conformational dynamics in biomolecules via chemical exchange saturation transfer: a primer, J. Biomol. NMR 67 (2017) 243–271.
[8] B. Zhao, A.L. Hansen, Q. Zhang, Characterizing slow chemical exchange in nucleic acids by carbon CEST and low spin-lock field $R_{1\rho}$ NMR spectroscopy, J. Am. Chem. Soc. 136 (2014) 20–23.
[9] P. Vallurupalli, L.E. Kay, Probing slow chemical exchange at carbonyl sites in proteins by chemical exchange saturation transfer NMR spectroscopy, Angew. Chem. Int. Ed. Engl. 52 (2013) 4156–4159.
[10] G. Bouvignies, L.E. Kay, A 2D ^{13}C-CEST experiment for studying slowly exchanging protein systems using methyl probes: an application to protein folding, J. Biomol. NMR 53 (2012) 303–310.
[11] G. Bouvignies, P. Vallurupalli, L.E. Kay, Visualizing side chains of invisible protein conformers by solution NMR, J. Mol. Biol. 426 (2014) 763–774.
[12] P. Vallurupalli, G. Bouvignies, L.E. Kay, A computational study of the effects of ^{13}C–^{13}C scalar couplings on ^{13}C CEST NMR spectra: towards studies on a uniformly ^{13}C-labeled protein, ChemBioChem 14 (2013) 1709–1713.
[13] E. Rennella, R. Huang, A. Velyvis, L.E. Kay, $^{13}CHD_2$-CEST NMR spectroscopy provides an avenue for studies of conformational exchange in high molecular weight proteins, J. Biomol. NMR 63 (2015) 187–199.
[14] A.L. Hansen, G. Bouvignies, L.E. Kay, Probing slowly exchanging protein systems via $^{13}C^{\alpha}$-CEST: monitoring folding of the Im7 protein, J. Biomol. NMR 55 (2013) 279–289.
[15] B. Zhao, S.L. Guffy, B. Williams, Q. Zhang, An excited state underlies gene regulation of a transcriptional riboswitch, Nat. Chem. Biol. 13 (2017) 968–974.
[16] T. Yuwen, A. Sekhar, L.E. Kay, Separating dipolar and chemical exchange magnetization transfer processes in ^{1}H-CEST, Angew. Chem. Int. Ed. Engl. 56 (2017) 6122–6125.
[17] A. Sekhar, R. Rosenzweig, G. Bouvignies, L.E. Kay, Hsp70 biases the folding pathways of client proteins, Proc. Natl. Acad. Sci. USA 113 (2016) E2794–2801.
[18] T. Yuwen, R. Huang, L.E. Kay, Probing slow timescale dynamics in proteins using methyl ^{1}H CEST, J. Biomol. NMR 68 (2017) 215–224.
[19] T. Yuwen, L.E. Kay, Longitudinal relaxation optimized amide ^{1}H-CEST experiments for studying slow chemical exchange processes in fully protonated proteins, J. Biomol. NMR 67 (2017) 295–307.
[20] T. Yuwen, L.E. Kay, A new class of CEST experiment based on selecting different magnetization components at the start and end of the CEST relaxation element: an application to ^{1}H CEST, J. Biomol. NMR 70 (2018) 93–102.
[21] Q.L. Wu, B.A. Fenton, J.L. Wojtaszek, P. Zhou, Probing the excited-state chemical shifts and exchange parameters by nitrogen-decoupled amide proton chemical exchange saturation transfer (HN^{dec}-CEST), Chem. Commun. 53 (2017) 8541–8544.
[22] G.A. Morris, R. Freeman, Selective excitation in Fourier transform nuclear magnetic resonance, J. Magn. Reson. 29 (1978) 433–462.
[23] G. Bodenhausen, R. Freeman, G.A. Morris, A simple pulse sequence for selective excitation in Fourier transform NMR, J. Magn. Reson. 23 (1976) 171–175.
[24] T. Yuwen, L.E. Kay, G. Bouvignies, Dramatic decrease in CEST measurement times using multi-site excitation, ChemPhysChem (2018), https://doi.org/10.1002/cphc.201800249 (in press).
[25] A. Sekhar, J.A.O. Rumfeldt, H.R. Broom, C.M. Doyle, G. Bouvignies, E.M. Meiering, L.E. Kay, Thermal fluctuations of immature SOD1 lead to separate folding and misfolding pathways, Elife 4 (2015) e07296.
[26] A. Mittermaier, L.E. Kay, χ_1 torsion angle dynamics in proteins from dipolar couplings, J. Am. Chem. Soc. 123 (2001) 6892–6903.
[27] F. Delaglio, S. Grzesiek, G.W. Vuister, G. Zhu, J. Pfeifer, A. Bax, NMRPipe: a multidimensional spectral processing system based on UNIX pipes, J. Biomol. NMR 6 (1995) 277–293.
[28] D.F. Hansen, H.Q. Feng, Z. Zhou, Y.W. Bai, L.E. Kay, Selective characterization of microsecond motions in proteins by NMR relaxation, J. Am. Chem. Soc. 131 (2009) 16257–16265.
[29] K. Pervushin, B. Vogeli, A. Eletsky, Longitudinal ^{1}H relaxation optimization in TROSY NMR spectroscopy, J. Am. Chem. Soc. 124 (2002) 12898–12902.
[30] E. Lescop, P. Schanda, B. Brutscher, A set of BEST triple-resonance experiments for time-optimized protein resonance assignment, J. Magn. Reson. 187 (2007) 163–169.
[31] T. Kern, P. Schanda, B. Brutscher, Sensitivity-enhanced IPAP-SOFAST-HMQC for fast-pulsing 2D NMR with reduced radiofrequency load, J. Magn. Reson. 190 (2008) 333–338.
[32] D.W. Yang, K. Nagayama, A sensitivity-enhanced method for measuring heteronuclear long-range coupling constants from the displacement of signals in two 1D subspectra, J. Magn. Reson. 118 (1996) 117–121.
[33] M. Ottiger, F. Delaglio, A. Bax, Measurement of J and dipolar couplings from simplified two-dimensional NMR spectra, J. Magn. Reson. 131 (1998) 373–378.
[34] N.L. Fawzi, J. Ying, R. Ghirlando, D.A. Torchia, G.M. Clore, Atomic-resolution dynamics on the surface of amyloid-β protofibrils probed by solution NMR, Nature 480 (2011) 268–272.
[35] M.A. Smith, H. Hu, A.J. Shaka, Improved broadband inversion performance for NMR in liquids, J. Magn. Reson. 151 (2001) 269–283.
[36] H. Geen, R. Freeman, Band-selective radiofrequency pulses, J. Magn. Reson. 93 (1991) 93–141.
[37] P. Schanda, H. Van Melckebeke, B. Brutscher, Speeding up three-dimensional protein NMR experiments to a few minutes, J. Am. Chem. Soc. 128 (2006) 9042–9043.
[38] D. Marion, M. Ikura, R. Tschudin, A. Bax, Rapid recording of 2D NMR spectra without phase cycling. Application to the study of hydrogen exchange in proteins, J. Magn. Reson. 85 (1989) 393–399.
[39] M. Guenneugues, P. Berthault, H. Desvaux, A method for determining B_1 field inhomogeneity. Are the biases assumed in heteronuclear relaxation experiments usually underestimated?, J Magn. Reson. 136 (1999) 118–126.